Title	Microscopic particle discrimination using spatially-resolved Fourier-holographic light scattering angular spectroscopy
Author(s)	Hillman, Timothy R.; Alexandrov, Sergey; Gutzler, Thomas; Sampson, David D.
Publication Date	2006-11-13
Publication Information	Hillman, Timothy R., Alexandrov, Sergey A., Gutzler, Thomas, & Sampson, David D. (2006). Microscopic particle discrimination using spatially-resolved Fourier-holographic light scattering angular spectroscopy. Optics Express, 14(23), 11088-11102. doi:10.1364/OE.14.011088
Publisher	Optica
Link to publisher's version	https://dx.doi.org/10.1364/OE.14.011088
Item record	http://hdl.handle.net/10379/17138
DOI	http://dx.doi.org/10.1364/OE.14.011088

Microscopic particle discrimination using spatially-resolved Fourier-holographic light scattering angular spectroscopy

Timothy R. Hillman, Sergey A. Alexandrov, Thomas Gutzler, and David D. Sampson

Optical + Biomedical Engineering Laboratory,
School of Electrical, Electronic & Computer Engineering,
The University of Western Australia,
35 Stirling Highway, Crawley, Western Australia 6009, Australia

hillm-tr@ee.uwa.edu.au

http://obel.ee.uwa.edu.au

Abstract: We utilize Fourier-holographic light scattering angular spectroscopy to record the spatially resolved complex angular scattering spectra of samples over wide fields of view in a single or few image captures. Without resolving individual scatterers, we are able to generate spatially-resolved particle size maps for samples composed of spherical scatterers, by comparing generated spectra with Mie-theory predictions. We present a theoretical discussion of the fundamental principles of our technique and, in addition to the sphere samples, apply it experimentally to a biological sample which comprises red blood cells. Our method could possibly represent an efficient alternative to the time-consuming and laborious conventional procedure in light microscopy of image tiling and inspection, for the characterization of microscopic morphology over wide fields of view.

© 2006 Optical Society of America

OCIS codes: (070.0070) Fourier optics and optical signal processing; (090.0090) Holography; (100.2000) Digital image processing; (120.3890) Medical optics instrumentation; (170.1650) Coherence imaging; (170.3880) Medical and biological imaging; (170.4580) Optical diagnostics for medicine.

References and links

1. G. Sluder and D. E. Wolf, eds., *Digital Microscopy: a Second Edition of Video Microscopy* (Elsevier Academic Press, Amsterdam, 2003).
2. S. A. Alexandrov, T. R. Hillman, and D. D. Sampson, "Spatially resolved Fourier holographic light scattering angular spectroscopy," Opt. Lett. **30,** 3305–3307 (2005).
3. S. A. Alexandrov, T. R. Hillman, T. Gutzler, M. B. Same, and D. D. Sampson, "Particle sizing with spatially-resolved Fourier-holographic light scattering angular spectroscopy," in *BiOS 2006: Multimodal Biomedical Imaging,* F. S. Azar, D. N. Metaxas, eds., Proc. SPIE **6081,** 608104 (2006).
4. L. Yaroslavsky, *Principles of Digital Holography* (Kluwer Academic Publishers, Boston, 2003).
5. E. Cuche, F. Bevilacqua, and C. Depeursinge, "Digital holography for quantitative phase-contrast imaging," Opt. Lett. **24,** 291–293 (1999).
6. E. Cuche, P. Marquet, and C. Depeursinge, "Simultaneous amplitude-contrast and quantitative phase-contrast microscopy by numerical reconstruction of Fresnel off-axis holograms," Appl. Opt. **38,** 6994–7001 (1999).

7. G. Popescu, L. P. Deflores, J. C. Vaughan, K. Badizadegan, H. Iwai, R. R. Dasari, and M. S. Feld, "Fourier phase microscopy for investigation of biological structures and dynamics," Opt. Lett. **29,** 2503–2505 (2004).

8. P. Marquet, B. Rappaz, P. Magistretti, E. Cuche, Y. Emery, T. Colomb, and C. Depeursinge, "Digital holographic microscopy: a non-invasive contrast imaging technique allowing quantitative visualisation of living cells with subwavelength axial accuracy," Opt. Lett. **30,** 468–470 (2005).

9. M. Gustafsson and M. Sebesta, "Refractometry of microscopic objects with digital holography," Appl. Opt. **43,** 4796–4801 (2004).

10. M. Sebesta and M Gustafsson, "Object characterization with refractometric digital Fourier holography," Opt. Lett. **30,** 471–473 (2005).

11. B. Javidi, I. Moon, S. Yeom, and E. Carapezza, "Three-dimensional imaging and recognition of microorganism using single-exposure on-line (SEOL) digital holography," Opt. Express **13,** 4492–4506 (2005).

12. V. Mico, Z. Zalevsky, and J. Garcia, "Superresolution optical system by common-path interferometry," Opt. Express **14,** 5168–5177 (2006).

13. S. A. Alexandrov, T. R. Hillman, T. Gutzler, and D. D. Sampson, "Synthetic aperture Fourier holographic optical microscopy," Phys. Rev. Lett. **97,** 168102 (2006).

14. J. R. Mourant, T. M. Johnson, S. Carpenter, A. Guerra, T. Aida, and J. P. Freyer, "Polarized angular dependent spectroscopy of epithelial cells and epithelial cell nuclei to determine the size scale of scattering structures," J. Biomed. Opt. **7,** 378–387 (2002).

15. R. S. Gurjar, V. Backman, L. T. Perelman, I. Georgakoudi, K. Badizadegan, I. Itzkan, R. R. Dasari, and M. S. Feld, "Imaging human epithelial properties with polarized light-scattering spectroscopy," Nature Med. **7,** 1245–1248 (2001).

16. V. Backman, M. B. Wallace, L. T. Perelman, J. T. Arendt, R. Gurjar, M. G. Müller, Q. Zhang, G. Zonios, E. Kline, T. McGillican, S. Shapshay, T. Valdez, K. Badizadegan, J. M. Crawford, M. Fitzmaurice, S. Kabani, H. S. Levin, M. Seiler, R. R. Dasari, I. Itzkan, J. Van Dam, and M. S. Feld, "Detection of preinvasive cancer cells," Nature (London) **406,** 35–36 (2000).

17. K. Sokolov, R. Drezek, K. Gossage, and R. Richards-Kortum, "Reflectance spectroscopy with polarized light: Is it sensitive to cellular and nuclear morphology," Opt. Express **5,** 302–317 (1999).

18. H. Fang, M. Ollero, E. Vitkin, L. M. Kimerer, P. B. Cipolloni, M. M. Zaman, S. D. Freedman, I. J. Bigio, I. Itzkan, E. B. Hanlon, and L. T. Perelman, "Noninvasive sizing of subcellular organelles with light scattering spectroscopy," IEEE J. Sel. Top. Quantum Electron. **9,** 267–276 (2003).

19. A. Katz, A. Alimova, M. Xu, E. Rudolph, M. K. Shah, H. E. Savage, R. B. Rosen, S. A. McCormick, and R. R. Alfano, "Bacteria size determination by elastic light scattering," IEEE J. Sel. Top. Quantum Electron. **9,** 277–287 (2003).

20. W. P. Van De Merwe, J. Czégé, M. E. Milham, and B. V. Bronk, "Rapid optically based measurements of diameter and length for spherical or rod-shaped bacteria *in vivo*," Appl. Opt. **43,** 5295–5302 (2004).

21. N. N. Boustany, S. C. Kuo, and N. V. Thakor, "Optical scatter imaging: subcellular morphometry *in situ* with Fourier filtering," Opt. Lett. **26,** 1063–1065 (2001).

22. J. D. Wilson, C. E. Bigelow, D. J. Calkins, and T. H. Foster, "Light scattering from intact cells reports oxidative-stress-induced mitochondrial swelling," Biophys. J. **88,** 2929–2939 (2005).

23. J. D. Wilson and T. H. Foster, "Mie theory interpretations of light scattering from intact cells," Opt. Lett. **30,** 2442–2444 (2005).

24. Y. L. Kim, Y. Liu, R. K. Wali, H. K. Roy, M. J. Goldberg, A. K. Kromin, K. Chen, and V. Backman, "Simultaneous measurement of angular and spectral properties of light scattering for characterization of tissue microarchitecture and its alteration in early precancer," IEEE J. Sel. Top. Quantum Electron. **9,** 243–256 (2003).

25. Y. Liu, Y. L. Kim, and V. Backman, "Development of a bioengineered tissue model and its application in the investigation of the depth selectivity of polarization gating," Appl. Opt. **44,** 2288–2299 (2005).

26. M. Bartlett, G. Huang, L. Larcom, and H. Jiang, "Measurement of particle size distribution in mammalian cells *in vitro* by use of polarized light spectroscopy," Appl. Opt. **43,** 1296–1307 (2004).

27. Y. Liu, Y. L. Kim, X. Li, and V. Backman, "Investigation of depth selectivity of polarization gating for tissue characterization," Opt. Express **13,** 601–611 (2005).

28. A. Wax, C. Yang, R. R. Dasari, and M. S. Feld, "Measurement of angular distributions by use of low-coherence interferometry for light-scattering spectroscopy," Opt. Lett. **26,** 322–324 (2001).

29. R. N. Graf and A. Wax, "Nuclear morphology measurements using Fourier domain low coherence interferometry," Opt. Express **13,** 4693–4698 (2005).

30. J. Goodman, *Introduction to Fourier optics* (McGraw-Hill, New York, 1996, 2nd ed.).

31. A. Karlsson, J. He, J. Swartling, and S. Andersson-Engels, "Numerical simulations of light scattering by red blood cells," IEEE Trans. Biomed. Eng. **52,** 13–18 (2005).

32. J. C. Ramella-Roman, P. R. Bargo, S. A. Prahl, and S. L. Jacques, "Evaluation of spherical particle sizes with an asymmetric illumination microscope," IEEE J. Sel. Top. Quantum Electron. **9,** 301–306 (2003).

33. M. T. Valentine, A. K. Popp, D. A. Weitz, and P. D. Kaplan, "Microscope-based static light-scattering instrument," Opt. Lett. **26,** 890–892 (2001).

1. Introduction

In biological systems, it is often necessary to determine structural information over a large range of size scales. For example, the size and shape of individual cells and the distribution of these cells throughout a sample both represent important features necessary for tissue characterization. Histological analysis of tissue sections is the most informative way to assess cellular composition and events in many situations [1]. All such examinations are laborious tasks, particularly when large tissue areas must be surveyed to obtain statistically significant cell populations, yet information on the microscopic scale must be discerned in order to provide accurate characterization. Recently, our group proposed a new approach to perform high-throughput structural characterization of a wide range of biological samples [2, 3]. Our technique is based on the intrinsic dependence of the angular distribution of elastic light scattering upon sample microstructure. By employing digital Fourier holography, we seek to map, with a single camera exposure, scatterer sizes (and potentially refractive-index contrast) over exceptionally large fields of view. Ultimately, this technique could enable single-image-capture 'histological' assessment of the microscopic properties of millimeter-scale samples without histological staining and without microscopic examinations such as cell counting - indeed, without even resolving the scatterers. Our publications thus far have entailed the first proposal and demonstration of this technique [2], and a preliminary experimental and theoretical analysis [3]. In this paper, we present a thorough theoretical treatment of the technique, and for the first time demonstrate experimentally the ability of our approach to generate fully spatially-resolved particle size maps for non-biological samples, and spatially-resolved angular spectra of a biological sample. We finally discuss outstanding issues and limitations in its implementation.

The technology of digital holographic imaging has developed considerably in recent years [4] due to the accessibility of high-power personal computers and advances in digital recording hardware. Its primary advantage over alternative techniques is the ability to form a digital representation of the full complex field distribution of an image, thus enabling the application of image processing and reconstruction algorithms to extract sample features, without recourse to complex optical setups. The renewed impetus in the field has been particularly striking with respect to the application of digital holographic microscopy, and a considerable body of literature has developed. Published journal papers have included treatments of quantitative phase contrast microscopy [5, 6, 7, 8], refractometry [9, 10], three-dimensional visualization [11], and synthetic-aperture optical imaging to achieve superresolution [12], or high resolution over large fields of view while utilizing low-numerical-aperture optics [13].

In parallel with developments in digital holographic microscopy, methods of characterizing a sample using the angular distribution [14] or spectrum [15] of elastically scattered light have been developed. These techniques have been termed 'light scattering spectroscopy' (LSS) and have been developed to quantify cellular or subcellular morphology (structure). LSS has shown promise in the detection of nuclear pleomorphism (the increase in size and shape variation of cell nuclei associated with dysplasia) in epithelial tumors *in vivo* [15, 16, 17, 18] and has been applied to bacteria size determination [19, 20]. A closely related microscopy technique has combined LSS with optical Fourier filtering to map morphology over a microscope's field of view [21]. More recently, the importance of angular distributions has begun to be appreciated [22, 23], including the combined measurement of angular and spectral scattering distributions [24]. All such techniques are not intrinsically depth sectioning, which is a common important requirement for thick or turbid media. Both polarization gating [15, 16, 25, 26, 27] and coherence gating [28, 29] have been used to determine the depth-resolved spectral or angular distributions of scattered light.

In quantitative microscopy, the morphological parameters of samples are generally measured directly and accuracy depends largely on spatial resolution. The requirement for high spatial

resolution typically restricts fields of view to substantially less than the region of interest. In LSS, microscopic morphology and spatial resolution are decoupled; measurements averaged over small but macroscopic areas of the sample are sensitive to microscopic morphology. Accurate measurements of the scatterer sizes can still be obtained, via the convenient use of low-resolution optics. The angular scattering spectra published elsewhere [14, 19, 20, 22, 23, 24, 28] were obtained point by point over a sample area. Our technique enables such spectra to be collected over millimeter-scale samples with a single image capture.

The remainder of the paper is organized as follows. In Section 2, we describe in detail the theory of the technique. In Section 3, we present its experimental realization and an analysis of the experimental setup. In Section 4, we present experimental results. We provide some discussion and draw some conclusions in Section 5.

2. Methodology

To determine the angular scattering spectra for each local area of a sample, it is sufficient to record the complex amplitude distribution of the scattered wave. Our approach is based on recording a digital hologram of the scattered light in a plane optically conjugate to the Fourier plane of the object. By performing filtering in either the Fourier plane or the reconstructed object plane, we are able to generate spatially-dependent angular scattering profiles for the sample.
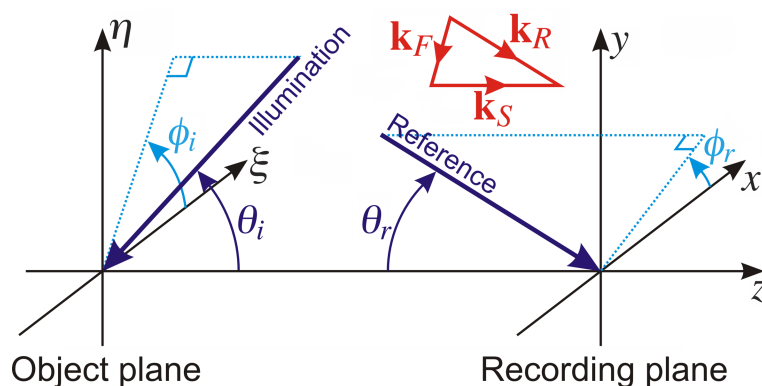

Fig. 1. Schematic showing orientation of the object and recording planes, and their coordinate systems. The wavevectors $\mathbf{k}_R$ and $\mathbf{k}_S$, and the fringe vector $\mathbf{k}_F$, correspond to the special case of an axial sample wave.

Figure 1 is a schematic showing the orientations of the object (ξ, η) and recording (x, y) planes, and the coordinate systems used to describe them. The complex representations of the Fourier transform of the scattered wave and the plane reference wave in the recording plane may be denoted $U_S(x,y) = U_{0S}(x,y)\exp[-j\varphi_S(x,y)]$ and $U_R(x,y) = U_{0R}\exp[-j\varphi_R(x,y)]$, respectively, where $U_{0S}(x,y)$ is a real (positive) spatially-varying amplitude, and U_{0R} is a constant amplitude (assumed real and positive, without loss of generality). The term $\varphi_S(x,y)$ is the phase of the Fourier transform of the sample wave, $\varphi_R(x,y) = k\sin\theta_r(x\cos\phi_r + y\sin\phi_r)$ is the phase of the reference wave, linear with respect to spatial position, $k = 2\pi/\lambda$ represents optical wavenumber, and λ is the wavelength of the source. The angle θ_r is the incident angle of the reference wave (relative to the z-axis, which is normal to the Fourier plane) and ϕ_r is the azimuthal angle, i.e., the angle between the reference plane of incidence and the x coordinate axis.

The recorded intensity distribution is:

$$I(x,y) = U_{0S}^2 + U_{0R}^2 + U_S U_{0R} e^{j\varphi_R} + U_S^* U_{0R} e^{-j\varphi_R}. \tag{1}$$

When this intensity is inverse Fourier-transformed, we obtain

$$\begin{aligned}\mathscr{F}^{-1}[I(x,y)] = & \; \Gamma_u(\nu_x, \nu_y) + U_{0R}^2 \delta(\nu_x, \nu_y) + U_{0R} u_S \left(\nu_x + \frac{\sin\theta_r \cos\phi_r}{\lambda}, \nu_y + \frac{\sin\theta_r \sin\phi_r}{\lambda} \right) \\ & + U_{0R} u_S^* \left(-\nu_x + \frac{\sin\theta_r \cos\phi_r}{\lambda}, -\nu_y + \frac{\sin\theta_r \sin\phi_r}{\lambda} \right),\end{aligned} \tag{2}$$

where $\mathscr{F}^{-1}$ denotes the inverse Fourier-transform operator, defined by the equation:

$$h(\nu_x, \nu_y) = \mathscr{F}^{-1}\{H(x,y)\} = \int_{-\infty}^{\infty} H(x,y) \exp\{+j2\pi(\nu_x x + \nu_y y)\}\, dxdy, \tag{3}$$

and (ν_x, ν_y) represent the coordinates in the transform space. In Eq. (2), u_S is the inverse Fourier transform of U_S, and δ represents the Dirac delta function. The first term on the right-hand side of the equation, $\Gamma_u(\nu_x, \nu_y) = u_S(\nu_x, \nu_y) \otimes u_S^*(-\nu_x, -\nu_y)$, is a zero-order autocorrelation and the second term is a high-intensity zero-order spot, located at the origin. The third and fourth terms are first-order twin images of the sample field and its (spatially inverted) complex conjugate, each translated in opposite directions due to the influence of the exponential carrier factors. If the first-order images are sufficiently spatially separated from the zero-order images, the squared magnitude of the entire transformed distribution yields reconstructed twin images of the scattered power from the sample. Otherwise, the first two terms can be removed by recording the sample and reference intensities separately, and subtracting both from Eq. (1).

The reconstructed field $u_S(\nu_x, \nu_y)$ is a scaled version of the scattered field distribution in the object plane. We denote the latter distribution by $V_O(\xi, \eta)$ (utilizing the input plane coordinate system), such that:

$$V_O(\xi, \eta) = \frac{-j}{M} u_S \left(-\frac{\xi}{M}, -\frac{\eta}{M} \right), \tag{4}$$

where M is a constant (with dimensions of squared length) dependent on the optical elements of the setup and proportional to the illumination wavelength.

An important issue to consider in reconstructing the sample field distribution is that of defocusing, in both the object and recording planes. The recording plane may be deliberately defocused (i.e., located in a plane which is *not* conjugate to the back focal plane of the Fourier-transforming objective lens) when imaging strongly diffracting sample structures. This ensures that any tightly-focused bright spots in the recording plane are spread out over many pixels, improving signal-to-noise ratio, and avoiding detector saturation. For the present purposes, recording plane defocusing is unnecessary, since the detected sample wave is generated by scattering processes. However, for each recorded hologram, there remains the possibility that the sample plane is defocused (not located at the front focal plane of the objective lens). Within the assumption of Fresnel diffraction theory, we can correct for this offset by multiplying the recording plane field U_S by a quadratic phase factor, as follows. If the sample is located at a distance g in front of the front focal plane, then the field in the front focal plane V_O is related to the field in the sample plane V_S via the convolution [30, p. 67]:

$$V_O(\xi, \eta) = V_S(\xi, \eta) \otimes k_g(\xi, \eta), \tag{5}$$

where:

$$k_g(\xi, \eta) = \frac{\exp(jkg)}{j\lambda g} \exp\left[\frac{jk}{2g}(\xi^2 + \eta^2) \right]. \tag{6}$$

Thus, U_S, the detected wave in the absence of defocus correction, is related to the defocus-corrected wave $U_{S,\mathrm{dc}}$ via the equation:

$$U_S(x,y) = U_{S,\mathrm{dc}}(x,y)K_g\left(-\frac{x}{M}, -\frac{y}{M}\right), \tag{7}$$

where K_g, the Fourier transform of k_g, may be represented:

$$K_g(\nu_\xi, \nu_\eta) = \exp\left(jkg\right)\exp\left[-jg\pi\lambda\left(\nu_\xi^2 + \nu_\eta^2\right)\right]. \tag{8}$$

If the recorded intensity distribution $I(x,y)$ is divided by the quadratic correction factor, we obtain (noting that the inverse of K_g is equal to its complex conjugate):

$$K_g^*I = U_{0S}^2 K_g^* + U_{0R}^2 K_g^* + U_{S,\mathrm{dc}}U_{0R}e^{j\varphi_R} + U_{S,\mathrm{dc}}^*(K_g^2)^*U_{0R}e^{-j\varphi_R}, \tag{9}$$

where the arguments of K_g are taken to be $(-x/M, -y/M)$ as in Eq. (7). It is clear from Eq. (9) that, after the recorded hologram is multiplied by the quadratic defocus correction factor, only one of the twin reconstructed images will be focused; the other will be doubly defocused.

The spatial (angular) frequency of the fringe pattern formed due to the interference between the sample and reference waves in the recording plane is calculated by projecting the difference between the sample and reference wavevectors, $\mathbf{k}_R$ and $\mathbf{k}_S$, respectively, onto the recording plane. For an axial sample wave, this difference, the fringe vector $\mathbf{k}_F = \mathbf{k}_R - \mathbf{k}_S$, is depicted along with $\mathbf{k}_R$ and $\mathbf{k}_S$ in Fig. 1. The wavevectors both have magnitude k and $\mathbf{k}_F$ has magnitude $k_F = 2k\sin(\theta_r/2)$. The fringe vector is oriented at angle $\theta_r/2$ to the recording plane, thus, its projection onto the plane has magnitude $k_F\cos(\theta_r/2)$. The spatial period of the fringe pattern is therefore:

$$H_f = \frac{2\pi}{k_F\cos(\theta_r/2)} = \frac{\lambda}{\sin\theta_r}. \tag{10}$$

It should be noted that in Fourier holography, this fringe period is not dependent on the scattering angle of the light from the sample; instead, it depends only on the location of the scatterer in the sample plane. This is an important advantage of Fourier holography over other techniques, endowing it with the ability to record a large range of scattering angles on a low-resolution CCD sensor.

For a sample composed of discrete scatterers, angular scattering spectroscopy measurements may be sufficient to ascertain the scatterers' sizes and their relative refractive indices with respect to the background medium. In the Fourier plane, there is a one-to-one correspondence between spatial position and scattered light direction. To determine the angular scattering distributions for selected sample regions, we have adopted two different (but essentially equivalent) techniques. In the first, we perform Fourier filtering using a selection of masks in the recording plane, each of which specifies (and weights) a particular scattering solid angle range. After filtering, a reconstructed image of the entire sample is formed only from the light scattered within that range. For each area of the sample, the variation in the reconstructed power corresponding to different mask positions can be used to determine sample structural characteristics. This technique, demonstrated in Refs. [2, 3], is useful when it is not convenient to select (manually or automatically) *a priori* sample regions of interest. In the second technique, we select such sample regions from the reconstructed object plane field distribution (where all detected scattering angles are utilized to form the reconstruction). The field within each region is Fourier-transformed to obtain a map of the scattering angle distribution. The principal advantage of this technique is the fact that it allows direct access to these two-dimensional maps. The distribution of the scattered power in each may be used to determine sample properties within the selected region.

The fundamental resolution limit of our method, which holds for both approaches above, is governed by the Fourier uncertainty relationship between angular resolution in the recording plane and spatial resolution in the sample plane. Assuming a (one-dimensional) Gaussian filter mask profile in the recording plane of full-width-at-half-maximum (FHWM) Δw, then according to Eq. (4), the spatial resolution in the reconstruction plane is limited by a Gaussian coherent point-spread function FWHM of $\Delta d = 4(\ln 2)M/(\pi \Delta w)$. In the paraxial approximation, the deflection angle θ_d (from the optical axis) is related to the focal point deflection distance in the recording plane r_d by the equation $\theta_d = \lambda r_d/M$. Thus, the scattering angle resolution (FWHM in air) $\Delta \theta$ is related to spatial resolution in the reconstruction plane Δd by the equation:

$$\Delta d \Delta \theta = \frac{4\ln 2}{\pi}\lambda.\qquad(11)$$

It is clear from Eq. (11) that the only system parameter upon which the trade-off depends is the optical wavelength. For the red He-Ne laser wavelength $\lambda = 632.8$nm and a FWHM angular resolution of $\Delta \theta = 1.0°$, this yields a sample spatial resolution $\Delta d = 32\mu$m. Despite the fact that this value is clearly too large to directly resolve sample microstructure, it does not represent an impediment in our approach.

3. Experimental setup and procedure

Figure 2 presents a schematic diagram of our experimental setup. A light beam from a coherent source S (He-Ne laser) is split into reference and sample waves at the beamsplitter B1. A sample is placed at the object plane of the Fourier-transforming objective lens L1 (focal length $f_1 = 15$mm) and illuminated by a plane wave. Its optical Fourier spectrum is imaged onto the recording plane via the lenses L2 and L3 (of focal lengths $f_2 = 15$cm and $f_3 = 26$cm, respectively). For this setup, the scaling constant $M = \lambda f_1 f_3/f_2$. Recording is performed using a charge-coupled device (CCD) matrix sensor (12 bit, 1392×1040 pixels, pixel length $\Delta r = 4.65\mu$m). The reference wave is expanded using the telescopic system T and is directed off-axis onto the CCD matrix at angle θ_r of approximately 2.3°.
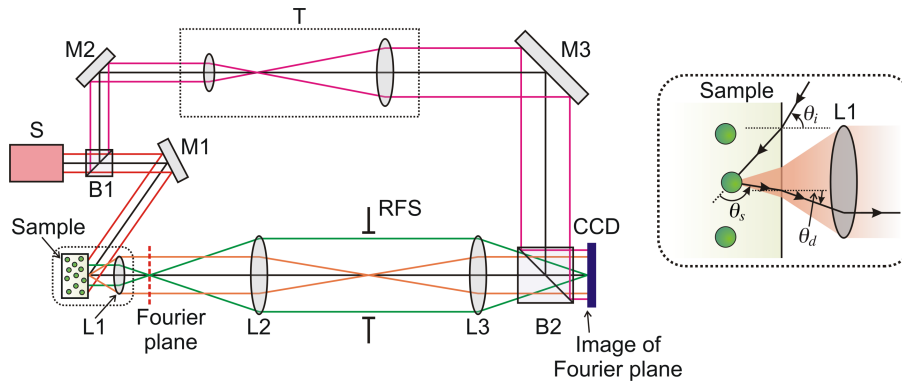

Fig. 2. Schematic diagram of the experimental setup. Items L1, L2, L3 are lenses, M1, M2, M3 are mirrors, B1, B2 are beamsplitters, RFS is a rectangular field stop, S is the light source, T is a telescopic system, and CCD is the CCD matrix sensor. The inset contains a magnified depiction of the sample, showing the direction of the illumination and scattered waves within the sample plane.

The direction of the light scattered by the sample is described by a polar (scattering) angle θ_s, the deviation from the forward direction, and an azimuthal angle. Its angular deviation θ_d

from the axis depends on both of these angles, as well as the direction of the illumination wave (described by θ_i, ϕ_i) and the refractive index of the sample medium n_{med}. The inset to Fig. 2 illustrates this relationship in the plane of incidence. Restricting our consideration to this plane, we may let θ_d take both positive and negative values with respect to the optical axis, with the direction shown corresponding to a positive value. Within this plane, θ_s is related to θ_d via the equation:

$$\theta_s = \pi - \left[\arcsin\left(\frac{\sin\theta_i}{n_{\text{med}}} \right) + \arcsin\left(\frac{\sin\theta_d}{n_{\text{med}}} \right) \right]. \tag{12}$$

The range of angles captured by the optical system is limited by the numerical aperture (NA) of the objective lens L1, the diameters and focal lengths of lenses L2 and L3, and the pixel size and count of the CCD sensor. In our case, the size of the CCD sensor is (for the most part) the limiting component of the system. For our experimental setup, in which $\theta_i \cong 49°$, the angular deviation θ_d range is about 17° (in air), centered on the axis. If the sample background medium is water ($n_{\text{med}} = 1.33$), the scattering angles θ_s which can be detected range from 139° to 152°. A rectangular field stop is placed in a plane conjugate to the sample, in order to restrict the field of view to a 1mm×2mm area, thus enabling clear identification of the first-order twin images.

The precise relationship between recording plane location and scattering direction can be determined. For our setup, the ξ, η, x, and y axes, depicted in Fig. 1, are aligned with the horizontal and vertical axes of the CCD recording area, respectively, and the azimuthal angle $\phi_i \cong 35°$. For our system parameters, curves in the recording plane corresponding to constant scattering angle θ_s (but varying azimuthal angle) are displayed in the left panel of Fig. 3. The curves are well approximated by straight lines perpendicular to the illumination-wave plane of incidence (in the paraxial approximation), i.e., oriented at angle ϕ_i to the y-axis. (The angular error associated with this straight-line approximation is less than 0.2° over virtually the entire recording plane.) The distance between two such lines corresponding to a scattering angle difference of $\theta_{s,\text{diff}}$ is approximately $\tilde{x}_{\text{diff}} = (Mn_{\text{med}}/\lambda)\theta_{s,\text{diff}}$.
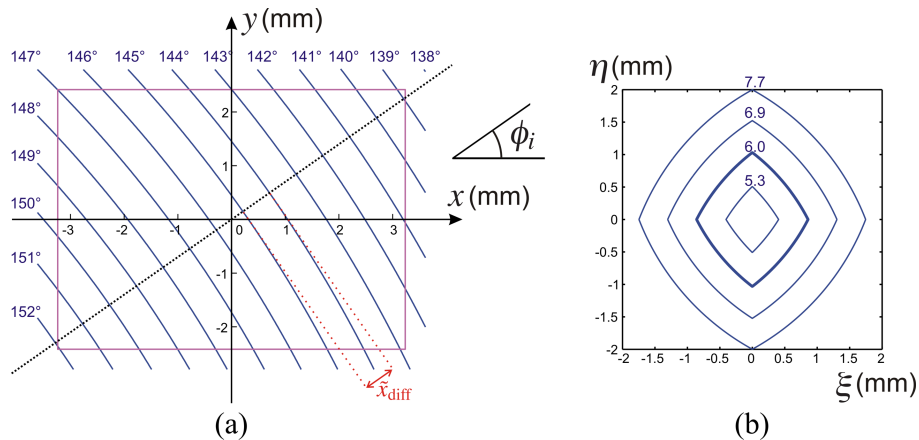

Fig. 3. (a) Curves of constant scattering angles in the recording plane. The distance $\tilde{x}_{\text{diff}}$ is shown for the case $\theta_{s,\text{diff}} = 1°$; (b) Regions in the sample plane for which the recorded spectrum is not limited by vignetting, for different objective lens diameters D_L (displayed in millimeters on each curve). In increasing order, their numerical apertures are 0.175, 0.2, 0.225 and 0.25. The case corresponding to our objective lens ($D_L \cong 6$mm) is highlighted.

Vignetting due to the optical components between the sample and recording planes can limit the sample field of view. We assume that the objective lens most severely limits the range of

scattered rays that can be detected by the system. Then the region of the Fourier spectrum (in the recording plane) contributed to by a scatterer at point (ξ_s, η_s) in the sample plane is a circle centered at the point $(x_s, y_s) = (f_3/f_2)(\xi_s, \eta_s)$ of diameter $(f_3/f_2)D_L$, where D_L is the diameter of the objective lens. Consider the sample area for which the CCD recording area lies entirely within this region. If the CCD recording area was circular with diameter D_R, then this area would also be a circle with diameter $D_S = D_L - (f_2/f_3)D_R$ (if $D_L > (f_2/f_3)D_R$, and zero otherwise). Of course, for our setup, the recording area is rectangular, with dimensions 4.8×6.5 mm. The corresponding sample areas for a range of different objective lens diameters are shown in the right panel of Fig. 3. For our case, the objective lens diameter $D_L \cong 6$mm, so that its NA was 0.2.

Let d_s be the diameter of the sample (or an alternative representative length). Then to ensure that the twin reconstructed images are spatially separated from the zero-order terms, it is necessary that [30, p. 309]:

$$\sin \theta_r \geq \frac{3d_s \lambda}{2M}. \tag{13}$$

To satisfy sampling restrictions due to the finite pixel size in the recording plane, it is necessary that $H_f > 2(\Delta r/\sqrt{2})$, where the factor $\sqrt{2}$ arises due to the effective pixel size in a diagonal direction, and the factor 2 arises from Nyquist's theorem, i.e., by Eq. (10):

$$\sin \theta_r < \frac{\lambda}{\sqrt{2}\Delta r}. \tag{14}$$

For a 1-mm-diameter sample, Eqs. (13) and (14) imply that, for our system, it is necessary that $3.3° \leq \theta_r < 5.5°$. Our choice of $\theta_r = 2.3°$ clearly violates the lower limit, so there will be some overlap between the zero-order terms and the twin images. As explained above, however, this can be overcome by digitally subtracting the recorded reference and sample waves from the hologram. Equation (13) demonstrates that, for a given CCD sensor size and wavelength, if d_s is increased, then M must undergo a corresponding increase to satisfy the inequality. That is, there is a trade-off between measured scattering angle range and sample size.

We selected samples based on their scattering profiles in the range of scattering angles θ_s detectable by our system, from about 139° to 152° as described above. The choice of microsphere suspensions was natural since their angular scattering pattern follows a distinctive modulation (ripple) pattern described by Mie theory, with an (angular) period which (for the most part) decreases with increasing sphere diameter. Our samples comprised polysterene spheres suspended in distilled water. The microspheres were diluted to a volume concentration of 0.1% and a droplet was deposited into a 10×20 mm well on a microscope slide. To demonstrate the application of our approach to biological samples, we utilized a smear of erythrocytes, or red blood cells (RBCs). The RBCs were diluted with a droplet of NaCl solution (9%) and evenly smeared over a microscope slide. A coverslip was placed over the sample, and sealed at the edges. The normal RBC shape is a discocyte, an axially-symmetric disc indented on the axis [31]. This shape produces a distinctive angular scattering ripple pattern [31] which should be clearly observable over our angle range.

For spherical scatterers, the angular scattering distribution depends on scattering angle but not significantly on azimuthal angle, and this fact was utilized when processing the images. When applying the first technique of Section 2, the recording plane masks were chosen to be strips perpendicular to the dotted line in Fig. 3(a). Each thereby corresponded to a single scattering angle (and the full range of azimuthal angles). (The filters had a Gaussian cross-section.) By applying a range of such masks to the recorded image, it was possible to record the total power scattered at each scattering angle. We were thus able to generate a one-dimensional curve of scattered power vs. scattering angle for each selected sample region [2]. When applying the

second technique, we sought to develop scatterer identification methods that were sensitive to structure parallel to the dotted line of Fig. 3(a) (in the scattering-angle-distribution map for each selected region), the direction of varying scattering angle.

4. Results

The scattered power angular distributions predicted by Mie theory are shown as blue curves in Fig. 4, assuming a refractive index ratio between sphere and background medium of $m = n_{sph}/n_{med} = 1.59/1.33 = 1.20$, for a range of particle sizes. The ripple patterns are readily
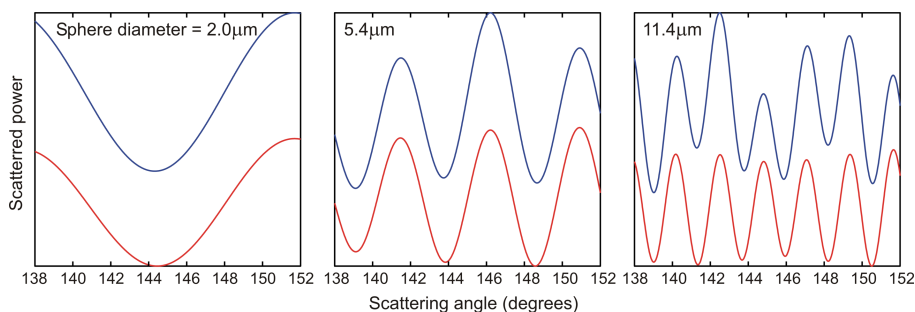
Fig. 4. Blue curves show scattered power vs. angle predicted by Mie theory; the high-pass filtered red curves emphasize their sinusoidal character. Each graph has an arbitrary (and different) scale on the ordinate axis.

apparent, as well as the dependence of their angular periods on sphere size. It is this parameter of the curves that we utilize to determine sphere size in our samples. To assign a value to the apparent angular period in each case, a high-pass filter was applied to the curve in order to fit it accurately to a sinusoidal curve. The angular period was originally estimated from the average fringe spacing over the angle range $120° - 170°$, and the (4th-order Butterworth) filter cutoff frequency was equal to 0.75 times the estimated fringe frequency. The filtered curves are shown in red. They were fitted (in a minimum least-squares sense) to sinusoidal curves, and the frequencies recorded. By this process, it may be shown that the ripple angular frequency is almost linearly dependent on the Mie size parameter $\alpha = \pi d n_{med}/\lambda$, where d is the sphere diameter. Such an approximation is valid (at least) over the refractive index ratio range $m = 1.1 - 1.25$, yielding a maximum error in detected diameter of less than 1μm (for sphere sizes ranging from 1 to 20μm) and a mean error of about 0.2μm. A more direct Mie inversion procedure may be used for particle size/refractive index values outside these ranges. Thus, particle size can be recovered from the measured ripple angular frequency, to a degree of accuracy which should be sufficient for many applications. The minimum particle size measurable by our system can be estimated by determining the sphere diameter for which one full ripple cycle is visible over the angular range used. As is clear from Fig. 4, this minimum size is about 2μm, assuming m is within the given range. In general, the particle-size sensitivity of our approach is limited by angular range and refractive index to the same extent as alternative angular-scattering-spectroscopy techniques [14]. Goniometric measurements published in the literature have clearly shown multiple Mie-theory ripples associated with sphere diameters of less than 1 or 2μm [20, 22, 32].

Figure 5 demonstrates the application of Method 1 of Section 2 to a sample of 11.4-μm spheres in water. The apparent brightness of the scattering regions of the sample (right-hand side) is clearly dependent on the recording plane strip-mask position (shown on the left-hand side) and, thus, on scattering angle.
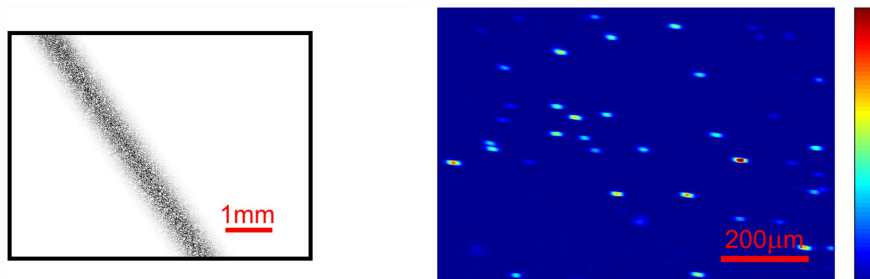
Fig. 5. Movie showing the variation in the reconstructed scattered power (right) as the recording plane strip-mask position (and corresponding selected scattering angle, left) is varied over a scattering angle range from 140° to 151°. (A low-pass spatial filter is applied to the reconstructed power map before it is displayed.) A linear gray or color scale is used for both parts of the figure. For the reconstructed power map, a false color scale is used; its color bar is depicted at the right of the figure.

Figures 6 and 7 show reconstructed images of samples of suspensions of 5.4 and 11.4-μm spheres in water, respectively. In each case, five regions of the sample were selected, and the angular scattering (power) spectra corresponding to each is displayed. Note that for each, the speckle size in the two-dimensional spectra (and thus the angular resolution) appears to be inversely related to the size of the selected region (outlined in red), an observation consistent with the trade-off represented by Eq. (11). A two-dimensional (inverse) Fourier transform operation was applied to each power spectrum, and the results also displayed, with a dotted yellow line indicating spatial frequencies in the direction of varying scattering angle. Bright spots along this line correspond to detected ripple frequencies in the angular scattering spectra, and by detecting the peak position (indicated with a magenta cross), we can identify each region with a detected sphere diameter by invoking the linear relationship described in the first paragraph of this section. (Diffraction effects due to the shape of the recording array and low-spatial-frequency noise were mitigated by subtracting a CCD-sensor-shaped rectangle from the spectra before inverse Fourier-transforming them, so that their mean value was zero, and applying a radial square-root-profile mask to the Fourier-transformed spatial frequency spectra before peak detection.) The same process was applied to every region of the sample, and the detected sphere size in each displayed using a false color scale. The color scale shown indicates sphere size in micrometers.

The mean diameter of the detected spheres (ignoring spurious outliers) was 4.8μm and 9.9μm (with standard deviations 0.9μm and 0.5μm), respectively. The systematic error of 10-15% is due possibly to errors in the system scaling constant M (due to the large tolerances of the optical components used), leading to a smaller range of scattering angles being imaged onto the CCD detector than predicted theoretically. The relatively large variation in the values measured in the former case is due to the difficulty in precisely detecting the period of low-frequency fringes using a detector encompassing a limited angular range. In both cases, the scatterers on the far left of the reconstruction take on a 'streaked' appearance. This is due to vignetting at the boundary of the sample region; the scatterers are reconstructed using a reduced range of spatial frequencies, so they exhibit a resolution loss (and apparent broadening) in one direction.

Figure 8 presents a reconstruction and a false-color map showing the detected size distributions of a sample containing a mixture of both 5.4 and 11.4-μm spheres. The two particle sizes are clearly distinguishable by their distinct hues used in the latter representation. Six different regions, three of each particle size, are highlighted as before. The detected sphere sizes are consistent with those measured in the previous two figures.
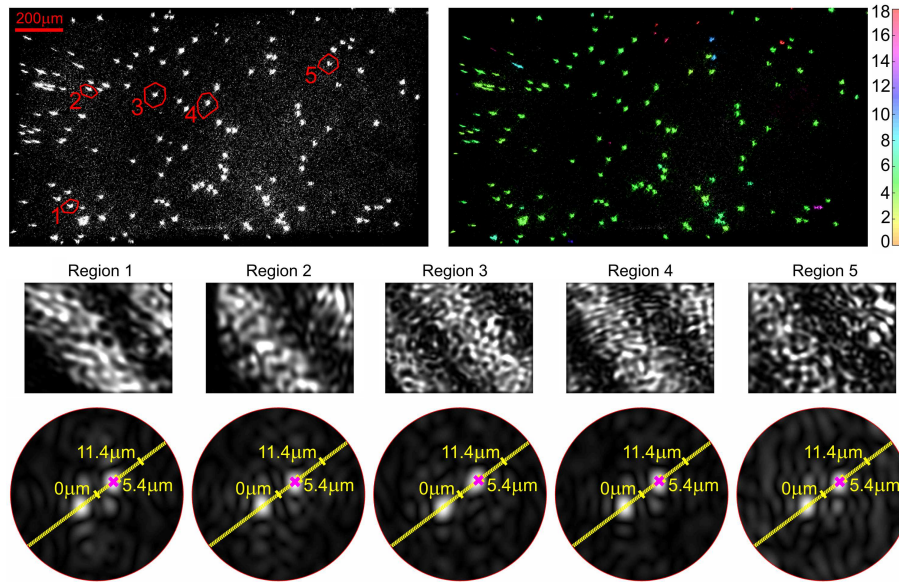
Fig. 6. Reconstruction of a sample of 5.4-μm spheres in water (logarithmic scale, top row, left), and a false-color plot (right) showing the detected sphere size in each region (the scale bar indicates sphere diameter in micrometers). The second row displays two-dimensional angular scattering power spectra (linear scale) corresponding to the five selected regions in the sample. The third row shows the two-dimensional inverse Fourier transform of each region (linear scale), with a dotted yellow line indicating the direction of scattering angle variation. The detected peak position is indicated with a magenta cross, and the theoretical peak positions corresponding to 5.4 and 11.4-μm spheres shown in yellow. The detected sphere sizes for the five regions were, respectively, 4.3, 4.3, 4.8, 4.6, and 4.3 μm.

The reconstructed image and scattering spectra from five selected regions of a hologram of the red-blood-cells sample are shown in Fig. 9. The orientation of the incident beam with respect to the recording plane was different from the previous measurements. (In this case, $\phi_i \cong 140°$.) Thus, the angle of the lines of constant scattering angle has been likewise varied. Clear ripple structure is apparent in the recorded power spectra (and highly visible peaks along the yellow dotted line in their inverse Fourier transforms), corresponding to a uniform spatial frequency. Since red blood cells are not spherical, it is not strictly appropriate to utilize Mie theory to determine their sizes. Nonetheless, for the purpose of comparison with the previous results, the same Mie inversion procedure was applied to the sample, and a false-color map of particle size generated, as before. (The fact that the relative refractive index m between the blood cells and their background was outside the range specified earlier in this section was ignored for the purpose of this simple analysis.) For this sample, despite the fact that a majority (65%) of detected particle sizes were within 1μm of the mean value (ignoring spurious outliers), there was much more variation in the detected blood cell sizes than in the sphere sizes of the earlier experiments. This is probably accounted for by the natural variation in the size and orientation of the particles, as well as the general inaccuracies inherent in applying a Mie-theory inversion procedure to a distribution of non-spherical particles. However, the mean detected size of about 6μm correlates well with typical red-blood-cell sizes reported in the literature [31]. It is evident in the reconstructed image (as it had been in Figs. 6-8) that the focused regions corresponding to individual red blood cells take the form of a pair of closely-spaced
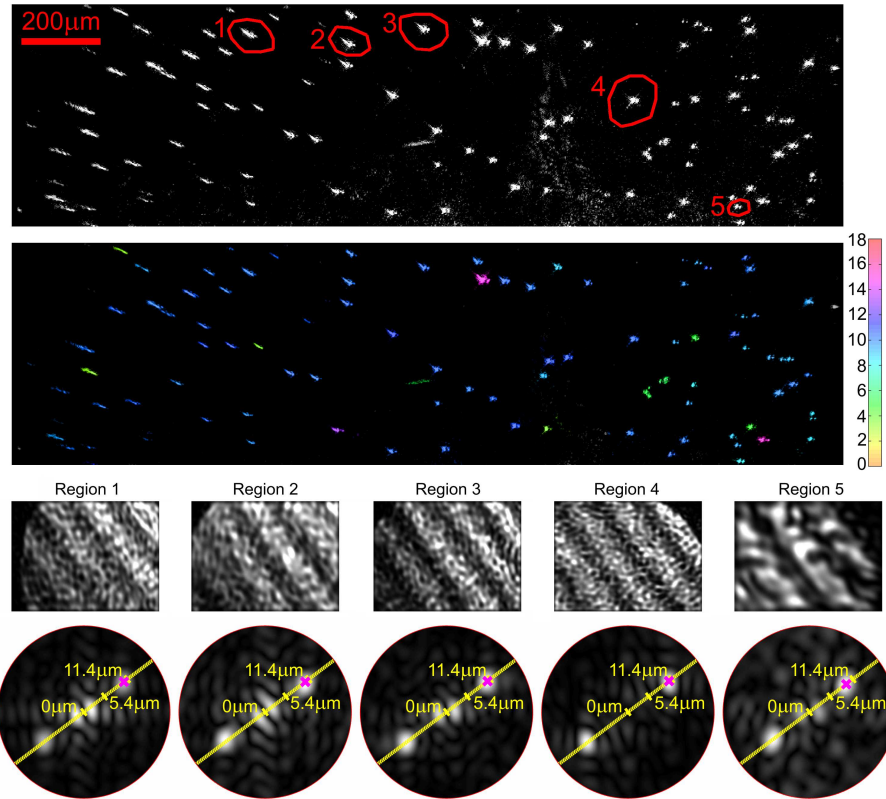
200μm

Region 1 Region 2 Region 3 Region 4 Region 5

11.4μm 11.4μm 11.4μm 11.4μm 11.4μm
0μm 5.4μm 0μm 5.4μm 0μm 5.4μm 0μm 5.4μm 0μm 5.4μm

Fig. 7. Reconstruction and sphere size detection of a sample of 11.4-μm spheres in water. The structure of the figure is similar to that of Fig. 6. The detected sphere sizes for the five regions were, respectively, 10.2, 10.2, 10.5, 10.5, and 9.4 μm.

bright points. This is unsurprising, since the far-field interference pattern generated by a pair of coherent point sources is a fringe pattern with a similar appearance to the two-dimensional spectra generated in these figures. We should therefore expect the focused scatterer images to be of this form when highly visible ripple patterns are present in the angular scattering spectra.

5. Discussion and Conclusion

The results presented in this paper clearly demonstrate the measurement of spatially resolved angular scattering spectra, and their use in estimating microscopic sphere sizes over large fields of view. We have confirmed that the spatial resolution required to resolve the sample's microstructure is not necessary to characterize it. The theoretical (diffraction-limited) spatial/angular resolution trade-off for the present setup (using a Gaussian-profile spatial filter mask) in the direction of varying scattering angle may be determined using Eq. (11). A representative pair of values is $\Delta\theta = 1.3°$ (in air), and $\Delta d = 25\mu$m. Utilizing the full mask length to reconstruct the sample, the angular/spatial resolutions in the direction of varying azimuthal angle are given by 8.9° (rectangular length) / 6μm (main lobe length). In principle, an image can be formed from a single exposure, in common with conventional microscopy, however, since we do not require spatial resolutions high enough to measure microparticle sizes directly, our system optical requirements are very modest. We can utilize a low-magnification,
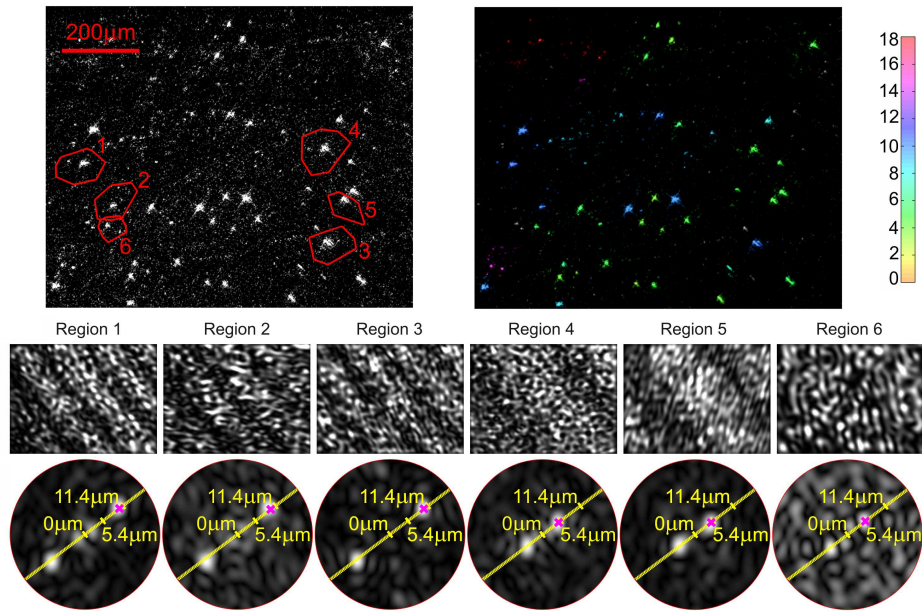
Fig. 8. Reconstruction and associated images of a sample comprising spheres of two different sizes (5.4 and 11.4μm) in water. The structure of the figure is similar to that of the previous two, except that six regions have been highlighted. Regions 1-3 correspond to the larger spheres, and regions 4-6 to the smaller spheres. The detected sphere sizes were 10.3, 10.0, 10.2, 4.8, 4.9, and 5.4 μm, respectively.

low-numerical-aperture objective, which allows us to form images over long working distances and millimeter-scale fields of view. This ability to form millimeter-scale images that provide the angular distribution of the scattered light in each local area is unique to our method.

Digitally recording the complex Fourier transformation of the scattered sample wave provides great flexibility for applying spatial filtering and, potentially, optical pattern recognition methods to select specific information from a sample. Besides Mie theory, other models to describe scattered light can be utilized in our technique. For example, for samples such as connective tissue that comprise non-spherical scatterers, alternative methods will be needed to quantify scatterer parameters. We are encouraged, in this regard, by the demonstrated sensitivity of light scattering to even small changes in the structure of a sample [21, 33]. In many instances, detection of change (e.g., differentiating normal from abnormal tissue structures) in itself will be sufficient to provide valuable capability. In our experiments, we used only the angular frequency of the Mie ripples to detect particle size. This parameter alone has low sensitivity to refractive index ratios (between spheres and background) over the range $m = 1.1 - 1.25$. If we were able to improve our processing procedure to consider other parameters such as peak position or relative magnitude, our approach could have even greater discriminatory powers. Curiously, even for samples composed of identical particles (as in Figs. 6, 7), the peaks in the one-dimensional scattering spectra were not aligned over the five images. This observation is partially accounted for by the variation in the size of the particles used (the manufacturer-specified standard deviation was 0.14 and 0.21μm, respectively, for the 5.4 and 11.4μm sphere sizes; diameter variations of about 0.3 and 0.2μm, respectively, would be sufficient to account for complete contrast reversal of the Mie ripples). Also, any variation in the particle shape from
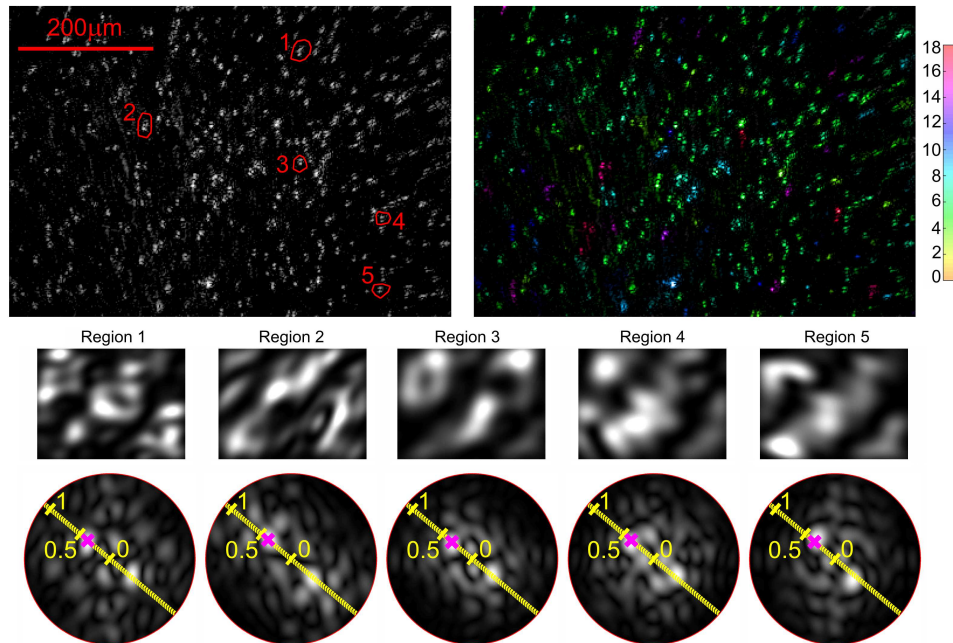
Fig. 9. Reconstruction and associated images of a sample of red blood cells. The structure of the figure is similar to that of the previous ones. The false-color size distribution was generated assuming that the particles could be approximated as spheres; the scale on the plots on the bottom row is not sphere diameter but fringe spatial frequency in inverse millimetres. The detected fringe frequencies were 0.37, 0.39, 0.34, 0.38, and 0.35 mm^{-1}, which would correspond to sphere diameters of 6.1, 6.3, 5.6, 6.2, and 5.7 μm, respectively.

sphericity could account for these anomalies.

The accuracy of the technique could be improved by collecting scattered light over a larger solid angle range, and we are currently working to achieve this (see, for example, Ref. [13]). The backscattering geometry that we use has the advantage of not detecting specularly reflected or undeflected incident light, but our scattering-angle range of sensitivity could in this way be extended three- or four-fold.

Spatially-resolved Fourier-holographic angular scattering spectroscopy has great potential for application to the study of the microarchitecture of biological tissue. The technique could provide maps of the size ranges of key scatterers, including cells, cell nuclei, and organelles, as well as the fibrous components of tissues such as collagen and elastin matrices.

Acknowledgments